

Morphology Formation Pathways in Solution-Processed Perovskite Thin Films

Martin Majewski, Olivier J.J. Ronsin, and Jens Harting*

The active layer in a perovskite solar cell is usually composed of a polycrystalline thin film. Fabrication of this layer by solution processing is a promising candidate for up-scaling to the mass market. However, the evolution of an evaporating and simultaneously crystallizing thin film is not yet fully understood. To contribute to the understanding of the formation of thin films, a geometrical model is developed that deals with the effect of the interplay between solvent evaporation and crystal growth on the dry film morphology. The possible film formation mechanisms are investigated, depending on the processing conditions. Eleven formation pathways are found leading to four distinct morphologies. It is shown how these formation pathways can be utilized by adapting the process parameters to the material properties. Pinhole-free and flat films can be fabricated if the evaporation rate is high in comparison to the crystal growth rate. Alternatively, providing a high crystal number density on the substrate can lead to the desired film morphology at low drying rates. The generality of the model makes it applicable to any evaporating and simultaneously crystallizing thin film.

PSK film growth is complex and involves sophisticated solution chemistry.^[7,8]

Different processing routes are possible, where deposition from solution is a promising candidate with potential for scale-up.^[9–11] In this approach, the physical processes that occur within a drying and simultaneously crystallizing film need to be understood. In principle, a mixture of precursor materials is dissolved, and a wet film is deposited on a substrate. Upon solvent evaporation, the precursor materials crystallize into perovskite. The perovskite crystals may form either directly, or the precursor materials may form crystalline intermediates with the solvent, from which the perovskite itself crystallizes in a second step.^[12,13] In this process, the amount of the intermediate phase primarily depends on the solvent.^[7] For weakly binding solvents, such as γ -Butyrolactone (GBL) or 2-Methoxyethanol (2-ME), the

transformation into perovskite was shown to be direct.^[5,14] In contrast, for strongly binding solvents, the intermediate phase quickly crystallizes and determines the final morphology.^[13,15,16] The specific formation pathway that results from a combination of solvents and a perovskite material system is an ongoing topic of research.^[17,18]

Experimentally, it was observed that a full substrate coverage and a low surface roughness are crucial for high-efficiency devices.^[19,20] In the case of the metal-halide perovskite materials used in printed photovoltaics, it was observed that drying has to be fast in order to obtain high-quality films, which might appear counter-intuitive. This highlights how crucial it is to understand how processing conditions, such as the initial precursor concentration, temperature, and evaporation rate, influence the film formation mechanisms and the final morphology.^[21,22] However, the morphology formation pathway is difficult to determine experimentally.^[23] It can be estimated using analytical models,^[24] such as the Lamer model,^[8,25] or through numerical simulations. Phase-field simulations allowed for describing the multi-component demixing of blends in drying films for organic photovoltaic systems.^[26–28] Similar methods were also applied to investigate the process-morphology relationships in meniscus-guided doctor blading for crystallizing films in the evaporative regime, and for immiscible blends in the Landau-Levich regime.^[29–31] Furthermore, evaporating crystallizing thin films were studied in the context of drug release.^[32–34] Recently, a theoretical description of the interplay between the nucleation and the evaporation rate of a thin film was proposed,^[35] while others developed a

1. Introduction

Perovskite (PSK) solar cells have the potential to become the next generation of solar cells, reaching the mass market.^[1,2] Their advantages include high power conversion efficiency, outstanding optoelectrical properties, and a low-cost, low-energy fabrication route.^[3] However, reliable deposition of high-quality films remains a challenge.^[4–6] Addressing this issue necessitates process design rules, based on physical understanding, for fully closed, large-area, smooth films. This is not straightforward as

M. Majewski, O. J. Ronsin, J. Harting
Helmholtz Institute Erlangen-Nürnberg for Renewable Energy (HIERN)
Forschungszentrum Jülich GmbH
Jülich, Germany
E-mail: j.harting@fz-juelich.de

J. Harting
Department of Chemical and Biological Engineering and Department of
Physics
Friedrich-Alexander-Universität Erlangen-Nürnberg
Fürther Straße 248, 90429 Nürnberg, Germany

 The ORCID identification number(s) for the author(s) of this article can be found under <https://doi.org/10.1002/advs.202516701>

© 2025 The Author(s). Advanced Science published by Wiley-VCH GmbH. This is an open access article under the terms of the [Creative Commons Attribution](#) License, which permits use, distribution and reproduction in any medium, provided the original work is properly cited.

DOI: 10.1002/advs.202516701

model for predicting the supersaturation rate, which is expected to drive perovskite crystallization in drying films.^[36] Nevertheless, the evolution of a doctor-bladed film in the Landau–Levich regime is not fully understood yet. Especially the necessity to dry fast in order to obtain a functional active layer in a perovskite solar cell, was unexpected.^[6]

To this end, our group developed a phase-field simulation framework^[37] that allows us to investigate the morphology formation of both organic^[38] and perovskite^[39] photo-active layers during wet film drying. We were able to validate the simulations by extensive comparison with experiments. Additionally, we found that the ratio of solvent evaporation rate to crystallization rate is the determining factor for the morphology formation. It has to be high in order to achieve a high-quality, smooth perovskite active layer.^[39] Furthermore, we showed that favoring perovskite growth from the substrate can also support the film quality. Thereby, it might become favorable to process at lower drying rates.^[40] In parallel to the simulations, analytical models need to be developed in order to obtain a broad and conclusive insight into the possible formation pathways.

Here, we develop a model that describes the growth of crystals located on the substrate in drying films. It allows for the identification of important events during film formation. The order in which they occur defines the formation pathway of the film and determines the final morphology. Although being very simplistic, the model allows us to establish generic guidelines for the real-world problem of depositing a smooth perovskite layer on a large area. Since no material-specific assumptions are made, these guidelines also apply to any other systems with similar properties.

In Section 2, we describe the assumptions underlying the model. Then, we discuss all the possible film formation pathways in the model in Section 3. In section 4, we explore the role of the drying rate and the crystal number density on the formation pathways and morphologies, and we connect our findings to the deposition of real films. In Section 5, we then examine the effects of the initial volume fraction of the wet film and of the initial crystal size. The paper concludes with a summary and an outlook.

2. Model

A precursor solution is deposited in a single step using a suitable method, such as doctor blading, spin coating, or slot-die coating. Immediately after deposition, the precursor materials are dissolved, and the film is a homogeneous liquid mixture. We consider the following two common experimental scenarios: First, the precursor solution is deposited on a substrate that is patterned with seeds. There is total control over the size and the place of all the seeds. Second, the precursor solution is deposited on a blank substrate. Heterogeneous nucleation at the substrate is ensured to be dominant compared to homogeneous nucleation within the film. In this case, the initial crystal sizes and the patterning density are statistically distributed and defined by the material properties. In this work, we represent heterogeneous nucleation through the average nucleation density and the critical radius. These properties, together with the processing conditions, define the final film morphology. In both cases, as the wet film subsequently dries, the wet film height decreases and the perovskite crystals grow from the substrate. The evaporation rate of

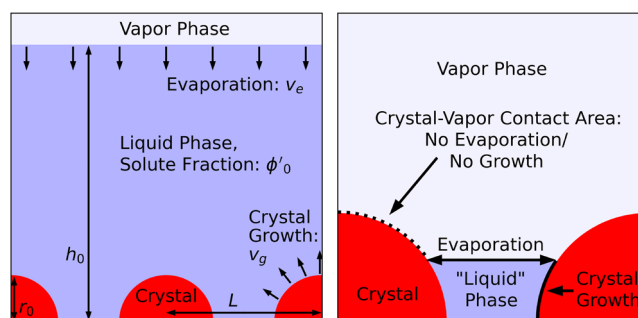


Figure 1. Left: Sketch of the initial state of the considered film, including model parameters. The vapor phase is shown in light blue, the liquid phase in dark blue and the crystalline phase in red. Right: Sketch of an intermediate state (zoom in) highlighting where crystal growth and solvent evaporation can take place. Note that the “liquid” phase on the right figure is composed of a mixture of liquid solvent, solvated and amorphous solute.

the solvent can be controlled (e.g., by gas quenching). The growth rate of the crystals is material-specific and therefore harder to modify. The initial volume and composition can be tuned up to the saturation threshold of the solute in the solvent.

Our model is designed to mimic this situation in a simplified manner. We consider the 2D cross-section of a drying film with half-spherical crystals initially located on an inert substrate and a vapor layer above it, as depicted in **Figure 1**. We investigate periodic arrangements of the crystals in the horizontal direction, with a unit cell consisting of two crystals of equal size and with equal distances between them. The evolution of both the crystalline and the liquid/amorphous phase can then be modeled. The liquid/amorphous phase is generally composed of one liquid solvent and one dissolved, amorphous solute. However, on the one hand, if crystallization consumes all the dissolved solute, the liquid phase becomes only composed of liquid solvent. On the other hand, if the whole solvent evaporates, this phase becomes composed of amorphous solute only, and is actually rather a non-liquid, but also non-crystalline, amorphous phase. In any of the three cases, we will hereafter refer to this part of the system as the “liquid phase” for simplicity, even if it is composed of pure solute. Note that the complex chemistry involved in perovskite crystallization, including intermediates and solid-state precursors is not taken into account, and the solute represents the material that eventually crystallizes into a perovskite structure. In the following we use the term “crystal” or “crystalline phase” for perovskite crystals. Only the solvent evaporates, while both the solute and crystalline phase cannot. The composition of the liquid phase is fixed initially but evolves with time. The liquid phase is assumed to always remain homogeneous, which implies that material transport is not diffusion-limited. The liquid-vapor interface displacement speed toward the substrate, arising due to evaporation, is hereafter referred to as the evaporation rate. Even if the evaporation rate of a drying mixture is not constant in general,^[41] for simplicity it is assumed here to be constant until evaporation fully stops, when there is no solvent left.

The crystalline phase is composed of pure solute and grows at a constant interface velocity (hereafter referred to as the crystal growth rate). Crystal growth consumes solute from the liquid phase. The equilibrium concentration of solute in the liq-

uid phase is assumed to be zero in the model for simplicity. Hence crystal growth globally terminates when the liquid phase consists of pure solvent only. In addition, crystal growth and evaporation stop locally wherever the crystal surface is exposed to air, as shown in Figure 1 (right). Surface tensions and/or wetting effects are not taken into account, so that the surface of the liquid phase is assumed to always remain flat. It is assumed that further nucleation during film drying is successfully avoided, so that crystallization proceeds only through growth of the initial seeds. The proposed picture is simple enough to be analytically tractable. Complexifying the model, for example by including diffusion-limited mass transport, and non-constant evaporation and growth rates, would quickly become analytically very challenging. However, phase-field simulations (see Section S8, Supporting Information) show that such refinements would not qualitatively change the findings presented in this work.

The model parameters are as follows: r_0 is the radius of the initially placed (half-spherical) crystals, h_0 is the initial height of the liquid film, and ϕ_0 is the initial fraction of solute in the condensed film. The distance between the centers of the crystals is given by L , while v_e and v_g describe the solvent evaporation rate and the crystal growth rate, respectively. These parameters are visualized in Figure 1 (left). In order to reduce the dimensionality of the parameter space, in the following we discuss the behavior of the drying film depending on the four independent parameters v_e/v_g , L/h_0 , r_0/h_0 and ϕ_0 .

The initial volume fraction ϕ_0 is defined as the volume fraction in the condensed film (which is the liquid and the solid phase). This may seem counter intuitive, but it has the advantage of simplified equations. In the case of dominant heterogeneous nucleation at the substrate, it is the volume fraction of the amorphous phase at the moment when the system is still liquid and the crystallization starts. This is likely to be higher than the initial coated volume fraction. In the case of seeded growth, it is the volume fraction of the complete amorphous phase, including the seed crystals, at the coating step. The volume fraction ϕ'_0 that has to be coated on top of the half circular seeds can be calculated by

$$\phi'_0 = \frac{2Lh_0\phi_0 - \pi r_0^2}{2Lh_0 - \pi r_0^2}. \quad (1)$$

Within this modeling picture, we can investigate the effect of geometry (film thickness, crystal spacing, and initial size) and global mass transfer between phases (evaporation and growth rate, initial solute amount) on the final morphologies. We can also find process design rules by relating the process-related model parameters to the film formation mechanisms and final morphologies.

3. Identification of the Possible Formation Pathways

Within the framework of the model introduced in the last section, we have identified four different events that may occur during evaporation and crystal growth, which sequence defines the formation pathway. The four events are the termination of evap-

Table 1. Formation pathways: The 11 formation pathways are listed according to the sequence of possible events E (end of evaporation), G (end of crystal growth), I (crystal impingement/“.” no impingement) and T (crystals touch the film surface). A sketch of the different formation pathways is given in Figure 2.

Number	First event	Second event	Third event	Fourth event
1	E	T	I	G
2	I	E	T	G
3	E	I	T	G
4	G	T	E	—
5	I	G	T	E
6	T	E	I	G
7	I	T	E	G
8	T	I	E	G
9	T	G	E	—
10	I	T	G	E
11	T	I	G	E

oration (abbreviation E, no solvent left in the liquid film), the termination of crystal growth (abbreviation G, no solute left in the liquid film), crystal impingement (abbreviation I), and the formation of a contact area between crystals and the vapor phase when the crystals touch the film surface (abbreviation T, see Figure 1), either because crystals grow so that their top surface reaches the surface of the condensed film, or because solvent evaporates so that the surface of the drying condensed film eventually exposes the top of the crystals to the air. Among these, crystal impingement is the only event that may not systematically occur, since growth might be insufficient for crystals to reach each other, as will be shown in detail below. These four events are sufficient and necessary to distinguish the possible formation pathways/morphologies that can occur in the model. They may be, in principle, sorted into $4! = 24$ different sequences. However, certain sequences are non-physical:

1. The event of crystals touching the film surface (T) requires either crystal growth or evaporation to be still ongoing processes. Thus, all sequences with T occurring after both events G and E are impossible.
2. Similarly, crystal impingement cannot take place if crystal growth is already terminated. Therefore, all sequences with event G occurring before event I are not possible. Note that sequences four and nine are possible; however, impingement does not occur: the morphologies resulting from these formation pathways feature pinholes.
3. When evaporation terminates before crystal growth, a layer of pure solute forms on the substrate. Consequently, there cannot be pinholes in the film and impingement necessarily occurs. This makes sequences with event E occurring before event G, and without event I, not possible.

This gives us 11 possible morphology formation pathways, which are listed in Table 1. In the following, we investigate in detail for which process and material parameters the various formation pathways take place, and to which morphologies they lead.

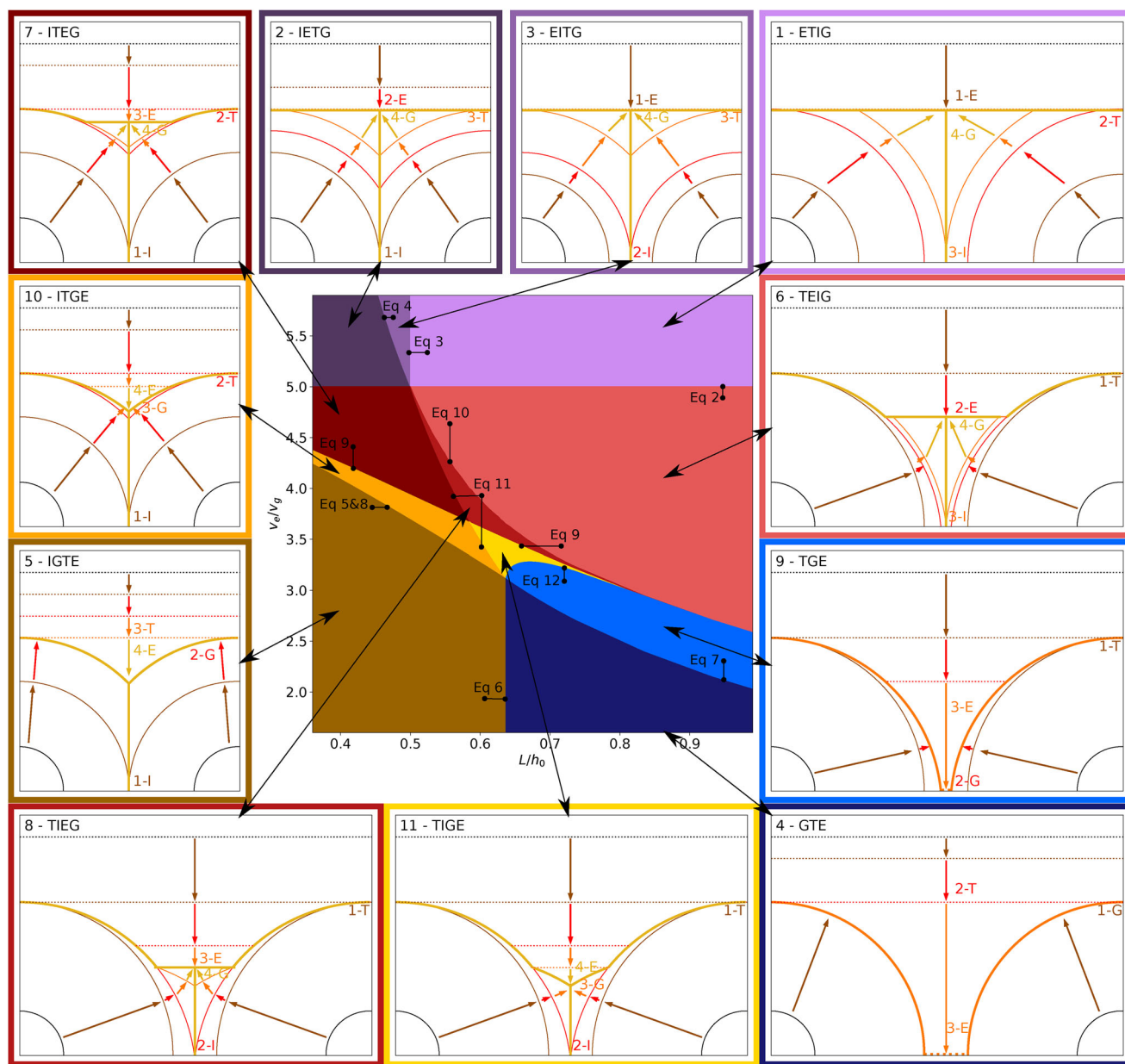


Figure 2. Center: The mapping of the formation mechanisms onto the parameter space. Each formation mechanism is represented by a different color. Each type of final morphology is represented by similar colors (e.g., light and dark blue for the morphology including pinholes). The equations from the main text used to distinguish the different sequences are connected to the respective limit. Surrounding: A sketch depicting the formation pathways of the classified morphologies. Only one interface between the crystals is shown. The formation pathways are connected to their place in the mapping. The occurrence of the four formation events, E: end of solvent evaporation, G: end of crystal growth, I: crystal impingement and T: contact between crystalline and vapor phase, are shown. The solid lines depict the extend of the crystalline phase and the dotted line the surface of the condensed film at the respective time step. The arrows indicate the temporal evolution of the system.

4. The Role of Drying Rate and Crystal Number Density

4.1. Identification of the Formation Pathways Depending on v_e/v_g and L/h_0

We aim at determining the boundaries between the different formation pathways depending on the drying rate and the crystal number density. More specifically, it turns out that the ra-

tio of evaporation to growth rate v_e/v_g , and of the distance between crystal centers to the initial film height L/h_0 are the two related parameters that best describe the existence of the formation pathways in the parameter space. The following section presents the conditions defining the existence domains of the formation pathways. The derivation of all the corresponding equations is provided in the Supporting Information, Sections S1 and S2. **Figure 2** provides an overview of the formation pathways in the 2D-parameter space $(L/h_0, v_e/v_g)$ at fixed initial volume

fraction ϕ_0 and ratio of initial crystal size to initial film height r_0/h_0 .

4.1.1. Fast Evaporation: Evaporation Finishes Before Crystals Touch the Film Surface ($E \rightarrow T \rightarrow G$)

Formation pathways no. 1, 2, 3: If evaporation is very fast as compared to growth (large v_e/v_g), evaporation may come to an end before crystal growth reaches the film surface (E before T). Since T may not occur after both E and G, the sequence of the three events needs to be ETG. For all of these sequences, evaporation ending before any crystal-vapor contact implies that the time for crystal growth up to the film surface is longer than the time for full solvent evaporation. Writing this condition as an equation and rearranging results in

$$\frac{v_e}{v_g} > \frac{(1 - \phi_0)}{\phi_0 - r_0/h_0}. \quad (2)$$

Note that this condition does not depend on L/h_0 , which implies a horizontal boundary in the 2D parameter space shown in Figure 2.

Nevertheless, three different formation pathways are possible, depending on when impingement occurs. Obviously, impingement occurs earlier when the crystals are initially closer to each other. This means that, in general, formation pathways corresponding to “early” impingement correspond to the lower L/h_0 ratios, and those corresponding to “late” impingement to the higher L/h_0 ratios. We begin with the case of “late” impingement, then consider the case of “early” impingement and finally discuss the intermediate formation pathway.

ETIG/no.1: in the case of “late” impingement, termination of evaporation (E) is the first step. As a result, the final state will be completely flat. Following this, the crystals grow up to the surface (T). They impinge (I), and growth eventually terminates when the film is fully converted to the crystalline state (G). The condition that the crystals first touch the film surface before impinging leads to

$$\frac{L}{h_0} > 2\phi_0. \quad (3)$$

Note that this condition does not depend on v_e/v_g , which implies a vertical boundary in the 2D parameter space in Figure 2.

IETG/no.2: in the case of “early” impingement, crystal impingement is the first event (I). Following this, evaporation terminates (E). Then, the crystals grow up to the film surface (T), and finally, crystal growth terminates when all the film is converted to the crystalline phase (G). This results in a final morphology similar to the previous one, characterized by no roughness and rectangular crystals. The condition that impingement occurs before the termination of evaporation leads to the following equation:

$$\frac{v_e}{v_g} < \frac{1 - \phi_0}{\frac{L}{2h_0} - \frac{r_0}{h_0}} \quad (4)$$

EITG/Nr.3: The final formation pathway corresponding to “intermediate” impingement is located between the two previous formation pathways in the 2D parameter space (see Figure 2).

Thereby, evaporation stops (E) before crystals impinge (I). Subsequently, the crystals grow to the surface (T) before crystal growth eventually stops (G).

4.1.2. Slow Evaporation: Crystal Growth Terminates Before the Crystal Touches the Surface ($G \rightarrow T \rightarrow E$)

Formation pathways no. 4, 5: If evaporation is very slow as compared to growth (small v_e/v_g), crystal growth may terminate while the crystals are still fully covered by solvent (G before T). Since T may not occur after both E and G, the sequence of the three events needs to be GTE. There is a maximal ratio of v_e/v_g for which growth ends before the crystal and the film surface touch each other. It is derived from the comparison between the time it takes to consume all the suitable material by crystal growth, and the time it takes for the liquid-vapor interface to travel down to the height h_{max} (top level of the fully grown crystals). This leads to

$$\frac{v_e}{v_g} < \frac{h_0 - h_{max}}{h_{max} - r_0}. \quad (5)$$

The maximum height of the crystals h_{max} depends on crystal geometry and thus on the occurrence of impingement.

GTE-(without I), no. 4: In this formation pathway, growth terminates first (G). Following this, the film surface touches the fully grown crystals due to continued evaporation (T). Finally, the evaporation stops when there is no solvent remaining (E). Impingement of the crystals is not even possible, so that the final morphology consists of two separated half-spherical crystals, with pinholes between them. The fact that the whole solute is contained in not-touching, half-spherical crystals, allows us to derive the first existence condition for this formation pathway:

$$\frac{L}{h_0} > \frac{8\phi_0}{\pi} \quad (6)$$

Due to the simple spherical geometry, the maximum crystal height can also be derived easily. This provides the second existence condition (on v_e/v_g) for this formation pathway as

$$\frac{v_e}{v_g} < \frac{1 - \sqrt{\frac{2L\phi_0}{h_0\pi}}}{\sqrt{\frac{2L\phi_0}{h_0\pi}} - r_0/h_0}. \quad (7)$$

IGTE, no. 5: In this formation pathway, corresponding to “early impingement,” impingement is actually the first event (I). Subsequently, crystal growth ceases when the solute volume is exhausted (G). The evaporation then causes the film surface to come into contact with crystals (T), and finally, the remaining solvent fully evaporates (E). The final morphology is pinhole-free and consists of impinged crystals with spherical caps. Evaluating the crystalline volume in this configuration, and knowing that it is equal to the total solute volume, allows us to calculate h_{max} by (numerically) solving the following equation (compare Section S2.3, Supporting Information):

$$\frac{L}{2} \cdot \sqrt{h_{max}^2 - (L/2)^2} + h_{max}^2 \arcsin\left(\frac{L}{2h_{max}}\right) = 2L \cdot \phi_0 \cdot h_0 \quad (8)$$

Inserting the value of h_{max} in Equation 5 provides the upper limit of the ratio of $(v_e)/(v_g)$ for which this formation pathway exists.

$$\frac{v_e}{v_g} < \frac{2 - L/h_0}{L/h_0 - 2r_0/h_0} \quad (11)$$

4.1.3. “Intermediate Fast” Evaporation: Evaporation Terminates Before Crystal Growth ($T \rightarrow E \rightarrow G$)

For these formation pathways (no. 6, 7, 8) evaporation terminates before crystal growth (E before G). Evaporation is not as fast as compared to the sequences considered in Section 4.1.1, so that the crystals and the film surface have sufficient time to touch before the solvent evaporation ends (TEG sequence). The upper existence limit along the v_e/v_g direction is given by Equation 2, beyond which the formation pathways discussed in Section 4.1.1 are active. The lower v_e/v_g limit separating them from the formation pathways at “intermediate slow” evaporation (see below) has to be solved for numerically. Thereby, we find the values for which the evolution of the amount of solvent

$$V_s(t) = 2L(1 - \phi_0)h_0 - v_e \cdot \frac{(h_0 - r_0)}{(v_g + v_e)} \cdot 2L - \int_{\frac{(h_0 - r_0)}{(v_g + v_e)}}^t dt (v_e \cdot (2L - 4\sqrt{(r_0 + v_g t)^2 - (h_0 - v_e \cdot t)^2}) \quad (9)$$

has a minimum at $V_s(t_{min}) = 0$. The origin of this condition is explained in detail in Section S2.4 (Supporting Information). Here again, we can distinguish three different pathways, depending on when impingement takes place. We discuss the case of “late” impingement first, then “early” impingement and finally the intermediate case.

TEIG, no. 6: For this formation pathway with “late” impingement, the crystals first come into contact with the film surface (T). Next, evaporation terminates (E). Subsequently, the crystals impinge (I), and the crystal growth stops (G). As a result, the shape of the crystals outside of the grain boundaries will no longer be spherical caps, because crystal growth continues only in the part of the crystal surface that remains covered by liquid. To distinguish this region from the remaining ones in this set, we use the fact that impingement happens later than the end of evaporation. We, therefore, solve for the ratio of v_e/v_g for which the impingement time is larger than the time t_s for the solvent to be fully evaporated,

$$t_i = \frac{L/2 - r_0}{v_g} > t_s, \quad (10)$$

where t_s is computed numerically (see details in Section S2.4, Supporting Information).

ITEG, no. 7: In this formation pathway, impingement occurs first (I), followed by the crystals’ contact with the (moving) film surface (T). Evaporation eventually ceases (E) earlier than the crystal growth (G). The resulting morphology is similar to the previous one. Additionally, a flat valley eventually forms in-between the crystals where the film surface stops at the end of evaporation. In order to identify the last limit for the existence of this pathway, we use the fact that impingement happens earlier than the formation of the crystal-vapor interface. This leads to

TIETG, no. 8: In this sequence with “intermediate” impingement, crystals first reach the vapor interface (T). This is followed by impingement (I), and finally, evaporation stops (E) a bit earlier than crystal growth (G). The resulting morphology is again similar to the previous ones.

4.1.4. “Intermediate Slow” Evaporation: Crystal Growth Terminates Before Evaporation ($T \rightarrow G \rightarrow E$)

For the last three evaporation pathways (no. 9, 10, 11), evaporation is slower than for the previous sequences. The first event is still the contact between crystals and film surface (T), but this time growth terminates before evaporation (TGE sequence). In the 2D parameter space shown in Figure 2, the existence region for the three remaining sequences is limited by Equation 7, and Equation 5 plus Equation 8 (from below) as well as Equation 9 (from above). Again, the three cases of “late,” “early,” and “intermediate” impingements have to be considered.

TGE-(without I), no. 9: For this sequence, the crystals first come into contact with the vapor interface (T). Subsequently, crystal growth stops (G), and finally, evaporation terminates (E). There is no impingement. The final morphology consists of distorted half-spheres with pinholes in between. The condition for the absence of impingement is also used to identify the existence region of this formation pathway, by solving numerically

$$\pi(r_0 + (h_0 - r_0)/(v_g + v_e) \cdot v_g)^2 + \int_{(h_0 - r_0)/(v_g + v_e)}^t dt (4 \cdot r(t) \arcsin\left(\frac{h_0 - v_e \cdot t}{r(t)}\right) \cdot v_g) = 2L(1 - \phi_0)h_0 \quad (12)$$

ITGE, no. 10: In this case, impingement happens first (I). Afterward, the crystals touch the film surface (T) and continue growing. The resulting crystal shape outside of the grain boundaries deviates from the spherical cap, as before. Now, crystal growth (G) stops earlier than evaporation (E). As a result, in this case, there is a trench instead of a flat valley in between crystals. Similar to the formation pathway ITEG, the difference we exploit to find the last existence limit for this sequence is that impingement happens earlier than the creation of a crystal-vapor interface. Here again, this leads to Equation 11.

TIGE, no. 11: For the final formation pathway, the crystals grow to the vapor interface (T) and then impinge (I). Crystal growth terminates (G) earlier than evaporation (E). Since crystal growth continues after the contact of the crystals with the vapor phase, the crystal shape developing before impingement deviates from being perfectly spherical. Due to impingement, there are no pinholes in this film. Between the crystals, there is a trench.

4.2. Morphologies and Process Design Rules

In summary, there are eleven possible formation pathways within the model’s hypotheses, leading to four types of morphologies.

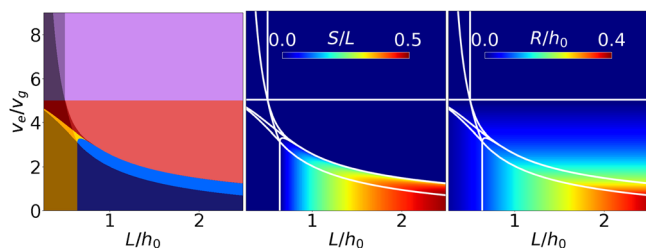


Figure 3. Analysis of substrate coverage and film roughness. Left: mapping of the formation pathways and morphology types based on the evaporation-to-growth rate ratio and the system size. Each formation mechanism is represented by a different color. Each type of final morphology is represented by similar colors. Center: The amount of uncovered substrate (S) between the crystals. Right: Roughness of the final morphology R, calculated as the ratio between the highest point of the film and the average film thickness. The definitions of the roughness and the amount of uncovered substrate are given in the Supporting Information, Sections S2.6 and S2.7. The boundaries between the formation pathways, obtained using the equations described in section 3, are indicated with white lines. For all the figures, the initial volume fraction of crystalline material is $\phi_0 = 0.25$, and the initial ratio of crystal size to film height is $r_0/h_0 = 0.1$ (same parameters as in Figure 2).

The first morphology arises when the ratio of drying rate to growth rate is high. For many slowly crystallizing systems, that may already be the case for medium or even low drying rates. The film is pinhole-free, perfectly flat, and consists of rectangular crystals. This morphology is created by the formation mechanisms 1, 2, and 3 (ETIG, IETG, EITG), corresponding to the purple regions in Figure 2. For the formation pathways 6, 7, 8 (TEIG, ITEG, TIEG) at “intermediate high” v_e/v_g , the film is pinhole-free but rough, with flat regions between the crystal domes. These morphologies are marked in red in Figure 2. For the formation pathways 5, 10, 11 (ITGE, IGTE, TIGE) at low v_e/v_g and low L/h_0 (high seed density), the film is still pinhole-free and rough, but with trenches between the crystal domes. These morphologies are marked in yellow in Figure 2. Finally, for the formation pathways 4 and 9 (GTE, TGE) at low v_e/v_g and high L/h_0 (low seed density), pinholes are present in the films between fully separated crystals. These morphologies are marked in blue in Figure 2.

We now turn to the evaluation of substrate coverage and film roughness in the dry film, depending on the film formation pathways (Figure 3). The existence regions of the different formation mechanisms with respect to v_e/v_g and L/h_0 are shown on the left. In the center, the amount of uncovered substrate is depicted. The roughness of the film, as defined by the ratio of the highest point in the dry film to the average film height, is shown on the right.

There are pinholes in the film only for the formation pathways 4 and 9. Thereby, the amount of uncovered substrate increases with increasing L/h_0 . The change in the amount of uncovered substrate between sequences 9 and 6 (light red) is quite drastic. This corresponds to the transition between pinholes, if crystal growth ceases earlier than evaporation, and an (infinitely) thin crystalline layer between the crystals, if evaporation ceases earlier than crystal growth.

The roughness of the dry films increases with increasing L/h_0 and decreasing v_e/v_g . For higher evaporation rates (lower growth rates), the crystals cannot grow far in the vertical direction, hence the roughness is lower. For a larger value of L/h_0 there is more

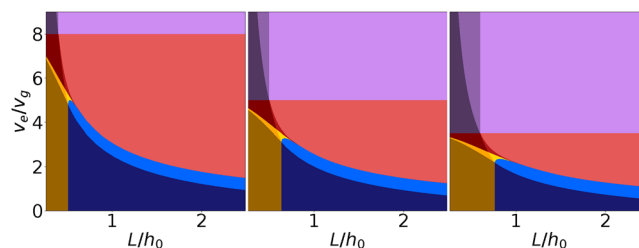


Figure 4. Mapping of the formation pathways and morphology types depending on initial volume fraction (ϕ_0). ϕ_0 increases from left to right ($\phi_0 = 0.2, 0.25, 0.3$). The initial ratio of crystal size to film height is $r_0/h_0 = 0.1$. Each formation mechanism is represented by a different color (the boundaries between the domains are calculated with the equations described in Section 3). Each type of final morphology is represented by similar colors.

crystalline material distributed on each crystal, allowing for a higher roughness. The film is expected to be perfectly flat only for sufficiently high v_e/v_g ratios.

From a practical perspective, the substrate should be fully covered with perovskite. Consequently, the region of the configuration space that should be strictly avoided is the blue region (sequences 4 and 9) appearing at low v_e/v_g and medium to high L/h_0 . That is one reason why a high seed density (corresponding to low L/h_0) or a high evaporation rate (high v_e/v_g) is advantageous for depositing the active layer of a high-performing solar cell.^[25,42,43] Note that perovskite materials often crystallize so fast that the desirable v_e may sometimes not be accessible experimentally. In such cases, using seeded growth or favoring heterogeneous nucleation on the substrate with a high seed number density (down-left part of the parameter space) might be an alternative.

On top of the mechanisms discussed in this work, further physical processes may take place in real systems. For instance, fast evaporation can lead to supersaturation in the liquid phase and thus trigger homogeneous nucleation in the film. This strongly influences the film morphology.^[39] Since a high evaporation rate promotes supersaturation and thus nucleation, there is a large number of crystals. The crystals arrange in such a way that the final film is relatively flat, which is positive. However, for device performance, a small amount of large crystals is preferred, because crystal boundaries lead to charge carrier recombination. To obtain a nearly smooth film surface with a small number of crystals (and therefore interfaces) and a low evaporation rate, an alternative formation pathway is to use a high seeding density (sequence 5, dark yellow). The roughness of the film also decreases with increasing seeding density (compare Figure 3).

5. The Impact of the Model Parameters

In this section, we investigate the effect of changing the two remaining relevant process parameters, the initial solute volume fraction ϕ_0 and the ratio of the initial crystal size to the initial film height r_0/h_0 . We first consider the effect of varying the initial volume fraction. To this end, three plots depending on v_e/v_g and L/h_0 with different initial volume fractions are shown in Figure 4. The roughness and the amount of uncovered substrate are shown in Section S3 (Supporting Information). The central plot corresponds to the parameters already used in Section 4.

Upon changes of the initial volume fraction, the pattern of the existence domains for the 11 formation pathways remains qualitatively unchanged. However, the exact location of the boundaries between the sequences shifts in response to changes in the initial volume fraction. A comparison of the three boundary representations reveals two notable effects: First, the boundaries shift toward lower ratios of v_e/v_g as the initial volume fraction increases. Second, the vertical boundaries shift toward larger L/h_0 .

The first effect can be understood qualitatively by considering that a higher initial solute volume fraction for the same initial film height means that the amount of solvent is lower. Consequently, evaporation does not need to be as fast to have the same effect as it would for a lower initial solute volume fraction. This leads to a downward shift of the boundaries for higher ϕ_0 . The second effect can be understood as follows: the interface position between a film with and without pinholes (compare Equation 6) and the interface at high evaporation rates (compare Equation 3) are directly proportional to ϕ_0 . For the interface at medium ratios of evaporation and growth rates, the effect is indirect. Equation 11 is independent of ϕ_0 , but the upper and lower limit for the evaporation to growth rates shifts to lower values (as explained before), and therefore these sequences seemingly shift to higher ratios of L/h_0 . Intuitively, one can think of the following: Given a higher initial volume fraction, there is more solute material in the system, resulting in larger crystals in the final state. This implies that larger distances between the crystals are required to produce a final film with pinholes/without impingement. This explains the shift toward larger L/h_0 for low v_e/v_g . For high ratios of v_e/v_g , the main difference is the increase in the (average) final film thickness, which increases the time until the crystal-air interface forms.

From a practical point of view, using a high evaporation rate may be experimentally complicated. Increasing the initial volume fraction allows for a reduction in the evaporation rate required to get a smooth film surface. Increasing the initial volume fraction also requires a lower seed density, at a low evaporation rate, to obtain a fully covered film.

Finally, we investigate the impact of the ratio of initial crystal size to initial film height r_0/h_0 . Domain existence representations corresponding to six different ratios r_0/h_0 are presented in Figure 5. The roughness and the amount of uncovered substrate are shown in Section S3 (Supporting Information). Here again, the central plot in the second line corresponds to the parameters already used in Section 4, and the pattern of the existence domains remains qualitatively unchanged. A comparison of the boundary representations reveals three notable features: First, for low ratios of r_0/h_0 , the boundaries between the existence domains remain (nearly) unchanged. Second, the boundaries between existence domains remain unchanged in the horizontal direction for any ratio. Third, increasing the ratio r_0/h_0 leads to a shift of the boundaries toward higher ratios of v_e/v_g .

This can be understood as follows: on the one hand, decreasing the initial crystal sizes increases the time the crystal needs to grow to a given size for the same crystal growth rate. To reach this size in the same amount of time, the growth rate must be larger, which means smaller v_e/v_g ratios. This is the reason why the boundaries shift to smaller v_e/v_g for smaller initial crystal sizes. This effect saturates when the initial crystal size becomes very small compared to the initial film thickness. On the other

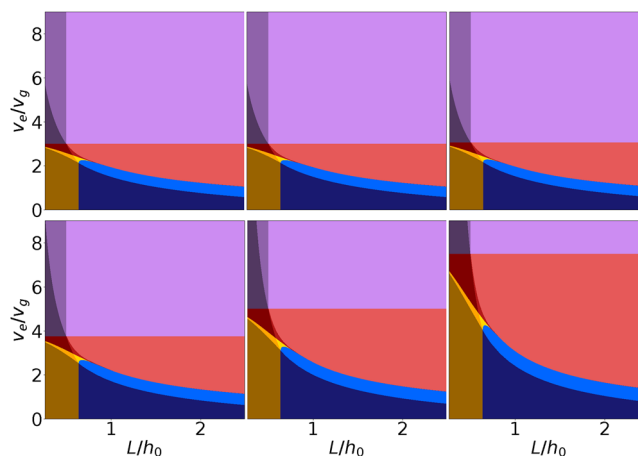


Figure 5. How the mapping of the formation pathways and morphology types changes with initial crystal size/initial film height variation. The ratio r_0/h_0 increases from left to right and top to bottom (first row: $r_0/h_0 = 5 \cdot 10^{-5}, 5 \cdot 10^{-4}, 5 \cdot 10^{-3}$ second row: $r_0/h_0 = 0.05, 0.1, 0.15$). The initial volume fraction is $\phi_0 = 0.25$. For very small ratios of r_0/h_0 the effect on the representation is negligible.

hand, the final crystal volume is the relevant parameter in determining the boundaries in the x-direction at low and high ratios of v_e/v_g . Since the initial solute volume fraction is calculated on the whole amorphous phase (including crystals), the change of crystal size does not change the amount of crystalline material (see Section 2). Hence, the boundaries do not move in the x-direction.

From a practical perspective, in the case of dominant heterogeneous nucleation at the substrate, the initial crystal size can be viewed as a simplified model for the critical radius, as described in the classical nucleation theory.^[6,44] According to this theory, there is a stable crystal size determined by a competition between interfacial and bulk energies. For perovskite solar cells, the system is in the regime of very low ratios of r_0/h_0 . Hence, changing the crystal size will not change the formation pathway. A slight increase in the initial film height corresponds to a movement to the left in the representation. Notably, the necessary ratio of evaporation to growth rate does not change.

For larger initial crystal sizes, we see that a larger critical radius requires a higher evaporation rate (or decreased growth rate) to produce a smooth film. Hence, it appears that a smaller initial crystal radius is favorable for the fabrication of smooth films because it allows for a reduced evaporation rate. An intuitive understanding of a change of the initial film height in this regime is complicated in this framework and is discussed in Section S4 (Supporting Information). In the case of controlled patterning with seeds, the seed size can be controlled. In this context, decreasing the seed size can be seen as a good way to favor the fabrication of smooth films, because the processing window in terms of evaporation rate becomes larger.

6. Summary and Outlook

A model was developed to describe the growth of perovskite crystals from the substrate in a drying solution. This allows for the investigation of how the interplay between evaporation and crystal growth determines the dry film morphology. We identified

four steps in the film formation: the impingement of the crystals, the formation of a contact line between the crystalline and vapor phase, the end of crystal growth, and the end of evaporation. The sequence of these events defines eleven possible formation pathways, leading to four different types of dry film morphologies that can be distinguished from each other, particularly regarding substrate coverage and film roughness. We found two possible ways to adjust processing parameters to obtain a final film with a smooth surface and full substrate coverage. We confirmed that the well-known approach using fast evaporation^[39] is a very effective way. More precisely, the evaporation rate has to be high enough compared to the crystal growth rate. This is the fundamental reason why the fast crystallizing metal-halide perovskites often require very fast drying. Another approach is to ensure a sufficiently high seed density at the substrate, which allows the use of low evaporation rates.

The proposed model has the advantage of being simple enough to be analytically tractable, and allows for the consideration of very basic physical properties of crystallizing film formation. While reality is more complex, we expect our findings to remain qualitatively valid even with further refinements and additional physics taken into account, such as surface tension effects, description of possible diffusion limitation, non-constant growth and evaporation rates, and generalization to 3D (see Chapter 8, Supporting Information). However, other processes, such as further nucleation during drying or multi-step crystallization through solid-state intermediates, could strongly affect the results of the model. Also the inhomogeneity of processing parameters may result in different sequences of the events, leading to different final morphologies in different areas of the film. At some point, the problem becomes so complex that simulations become necessary. In order to investigate the impact of these effects, the PF framework proposed by our group,^[37] which already describes evaporation, nucleation, growth and diffusion properties in detail, will be extended in the future to include dewetting effects and solid state precursors.

Supporting Information

Supporting Information is available from the Wiley Online Library or from the author.

Acknowledgements

The authors thank Kai Segadlo for helpful discussions and acknowledge financial support from the Deutsche Forschungsgemeinschaft (DFG) via the Perovskite SPP2196 programme (Project No. 506698391), the European Commission (H2020 Program, Project 101008701/EMERGE), and the Helmholtz Association (SolarTAP Innovation Platform).

Open access funding enabled and organized by Projekt DEAL.

Conflict of Interest

The authors declare no conflict of interest.

Data Availability Statement

The data that support the findings of this study are openly available in zenodo.org at 10.5281/zenodo.16673320, reference number 16673320.

Keywords

model, perovskite solar cell, thin film

Received: August 28, 2025
Revised: September 24, 2025
Published online: October 21, 2025

- [1] Best Research-Cell Efficiency Chart, <https://www.nrel.gov/pv/cell-efficiency.html>.
- [2] P. Zhu, C. Chen, J. Dai, Y. Zhang, R. Mao, S. Chen, J. Huang, J. Zhu, *Adv. Mater.* **2024**, *36*, 2307357.
- [3] L. Schmidt-Mende, V. Dyakonov, S. Olthof, F. Ünlü, K. M. T. Lê, S. Mathur, A. D. Karabanov, D. C. Lupascu, L. M. Herz, A. Hinderhofer, F. Schreiber, A. Chernikov, D. A. Egger, O. Shargaieva, C. Cocchi, E. Unger, M. Saliba, M. M. Byranvand, M. Kroll, F. Nehm, K. Leo, A. Redinger, J. Höcker, T. Kirchartz, J. Warby, E. Gutierrez-Partida, D. Neher, M. Stolterfoht, U. Würfel, M. Unmüßig, *APL Mater.* **2021**, *9*, 109202.
- [4] B. Parida, A. Singh, A. K. Kalathil Soopy, S. Sangaraju, M. Sundaray, S. Mishra, S. F. Liu, A. Najar, *Adv. Sci.* **2022**, *9*, 2200308.
- [5] X. Dai, Y. Deng, C. H. Van Brackle, J. Huang, *Int. J. Extreme Manuf.* **2019**, *1*, 022004.
- [6] W. A. Dunlap-Shohl, Y. Zhou, N. P. Padture, D. B. Mitzi, *Chem. Rev.* **2019**, *119*, 3193.
- [7] O. Shargaieva, H. Näsström, J. Li, D. M. Többens, E. L. Unger, *Front. Energy Res.* **2021**, *9*.
- [8] J. Jiao, C. Yang, Z. Wang, C. Yan, C. Fang, *Results Eng.* **2023**, *18*, 101158.
- [9] F. Yang, D. Jang, L. Dong, S. Qiu, A. Distler, N. Li, C. J. Brabec, H.-J. Egelhaaf, *Adv. Energy Mater.* **2021**, *11*, 2101973.
- [10] P. Wang, Y. Wu, B. Cai, Q. Ma, X. Zheng, W.-H. Zhang, *Adv. Funct. Mater.* **2019**, *29*, 1807661.
- [11] Q. Liu, W. Cai, W. Wang, H. Wang, Y. Zhong, K. Zhao, *J. Phys. Chem. Lett.* **2022**, 6503.
- [12] K. H. Stone, A. Gold-Parker, V. L. Pool, E. L. Unger, A. R. Bowering, M. D. McGehee, M. F. Toney, C. J. Tassone, *Nat. Commun.* **2018**, *9*, 3458.
- [13] A. M. Valencia, O. Shargaieva, R. Schier, E. Unger, C. Cocchi, *J. Phys. Chem. Lett.* **2021**, *12*, 2299.
- [14] C. Witt, K. Schötz, M. Kuhn, N. Leupold, S. Biberger, P. Ramming, F.-J. Kahle, A. Köhler, R. Moos, E. M. Herzig, F. Panzer, *J. Phys. Chem. C* **2023**, *127*, 10563.
- [15] K. Yan, M. Long, T. Zhang, Z. Wei, H. Chen, S. Yang, J. Xu, *J. Am. Chem. Soc.* **2015**, *137*, 4460.
- [16] J. Li, R. Munir, Y. Fan, T. Niu, Y. Liu, Y. Zhong, Z. Yang, Y. Tian, B. Liu, J. Sun, D.-M. Smilgies, S. Thoroddsen, A. Amassian, K. Zhao, S. F. Liu, *Joule* **2018**, *2*, 1313.
- [17] F. Ünlü, A. Florez, K. Dodd-Clements, L. K. Reb, M. Götte, M. Grosch, F. Yang, S. Öz, F. Mathies, S. Mathur, D. Ramirez, F. Jaramillo, E. Unger, *Adv. Energy Mater.* **2025**, *15*, 2403626.
- [18] B. M. Gallant, P. Holzhey, J. A. Smith, S. Choudhary, K. A. Elmetekawy, P. Caprioglio, I. Levine, A. A. Sheader, E. Y.-H. Hung, F. Yang, D. T. W. Toolan, R. C. Kilbride, K.-A. Zaininger, J. M. Ball, M. G. Christoforo, N. K. Noel, L. M. Herz, D. J. Kubicki, H. J. Snaith, *Nat. Commun.* **2024**, *15*, 10110.
- [19] G. Li, Z. Su, L. Canil, D. Hughes, M. H. Aldamasy, J. Dagar, S. Trofimov, L. Wang, W. Zuo, J. J. Jerónimo-Rendon, M. M. Byranvand, C. Wang, R. Zhu, Z. Zhang, F. Yang, G. Nasti, B. Naydenov, W. C. Tsai, Z. Li, X. Gao, Z. Wang, Y. Jia, E. Unger, M. Saliba, M. Li, A. Abate, *Science* **2023**, *379*, 399.
- [20] W. Qiu, T. Merckx, M. Jaysankar, C. M. de la Huerta, L. Rakocevic, W. Zhang, U. W. Paetzold, R. Gehlhaar, L. Froyen, J. Poortmans, D. Cheyns, H. J. Snaith, P. Heremans, *Energy Environ. Sci.* **2016**, *9*, 484.

- [21] S. Ternes, J. Mohacsi, N. Lüdtke, H. M. Pham, M. Arslan, P. Scharfer, W. Schabel, B. S. Richards, U. W. Paetzold, *ACS Appl. Mater. Interfaces* **2022**, *14*, 11300.
- [22] Z. Guo, A. K. Jena, G. M. Kim, T. Miyasaka, *Energy Environ. Sci.* **2022**, *15*, 3171.
- [23] O. Telschow, N. Scheffczyk, A. Hinderhofer, L. Merten, E. Kneschaurek, F. Bertram, Q. Zhou, M. Löffler, F. Schreiber, F. Paulus, Y. Vaynzof, *Adv. Sci.* **2023**, 2206325.
- [24] M. He, B. Li, X. Cui, B. Jiang, Y. He, Y. Chen, D. O'Neil, P. Szymanski, M. A. El-Sayed, J. Huang, Z. Lin, *Nat. Commun.* **2017**, *8*, 16045.
- [25] B. Ding, Y. Li, S.-Y. Huang, Q.-Q. Chu, C.-X. Li, C.-J. Li, G.-J. Yang, *J. Mater. Chem. A* **2017**, *5*, 6840.
- [26] V. Negi, O. Wodo, J. J. van Franeker, R. A. J. Janssen, P. A. Bobbert, *ACS Appl. Energy Mater.* **2018**, *1*, 725.
- [27] K. Zhao, O. Wodo, D. Ren, H. U. Khan, M. R. Niazi, H. Hu, M. Abdelsamie, R. Li, E. Q. Li, L. Yu, B. Yan, M. M. Payne, J. Smith, J. E. Anthony, T. D. Anthopoulos, S. T. Thoroddsen, B. Ganapathysubramanian, A. Amassian, *Adv. Funct. Mater.* **2016**, *26*, 1737.
- [28] O. Wodo, B. Ganapathysubramanian, *Comput. Mater. Sci.* **2012**, *55*, 113.
- [29] R. de Bruijn, A. A. Darhuber, J. J. Michels, P. van der Schoot, *Adv. Mater. Interfaces* **2025**, *12*, 2400556.
- [30] J. J. Michels, K. Zhang, P. Wucher, P. M. Beaujuge, W. Pisula, T. Marszalek, *Nat. Mater.* **2021**, *20*, 68.
- [31] R. de Bruijn, A. A. Darhuber, J. J. Michels, P. van der Schoot, *J. Chem. Phys.* **2024**, *161*, 194709.
- [32] C.-S. Kim, D. M. Saylor, M. K. McDermott, D. V. Patwardhan, J. A. Warren, *J. Biomed. Mater. Res., Part B* **2009**, *90B*, 688.
- [33] D. M. Saylor, J. E. Guyer, D. Wheeler, J. A. Warren, *Acta Biomater.* **2011**, *7*, 604.
- [34] D. M. Saylor, C. Forrey, C.-S. Kim, J. A. Warren, *Ann. Biomed. Eng.* **2016**, *44*, 548.
- [35] R. de Bruijn, J. J. Michels, P. van der Schoot, *J. Chem. Phys.* **2024**, *160*, 084505.
- [36] S. Ternes, F. Laufer, U. W. Paetzold, *Adv. Sci. n/a*, 2308901.
- [37] O. J. J. Ronsin, J. Harting, *Adv. Theory Simul.* **2022**, 2200286.
- [38] O. J. J. Ronsin, J. Harting, *ACS Appl. Mater. Interfaces* **2022**, *14*, 49785.
- [39] M. Majewski, S. Qiu, O. Ronsin, L. Lüer, V. M. L. Corre, T. Du, C. J. Brabec, H.-J. Egelhaaf, J. Harting, *Mater. Horiz.* **2025**, *12*, 555.
- [40] S. Qiu, M. Majewski, L. Dong, A. Distler, C. Li, K. Forberich, J. Tian, N. H. Hemasiri, C. Liu, J. Zhang, F. Yang, V. M. Le Corre, M. Bibrack, R. Basu, A. Barabash, J. Harting, O. J. J. Ronsin, T. Du, H.-J. Egelhaaf, C. J. Brabec, *Energy Environ. Sci.* **2025**, *18*, 5926.
- [41] O. J. J. Ronsin, D. Jang, H.-J. Egelhaaf, C. J. Brabec, J. Harting, *ACS Appl. Mater. Interfaces* **2021**, *13*, 55988.
- [42] X. Li, D. Bi, C. Yi, J.-D. Décoppet, J. Luo, S. M. Zakeeruddin, A. Hagfeldt, M. Grätzel, *Science* **2016**, *353*, 58.
- [43] F. Huang, Y. Dkhissi, W. Huang, M. Xiao, I. Benesperi, S. Rubanov, Y. Zhu, X. Lin, L. Jiang, Y. Zhou, A. Gray-Weale, J. Etheridge, C. R. McNeill, R. A. Caruso, U. Bach, L. Spiccia, Y.-B. Cheng, *Nano Energy* **2014**, *10*, 10.
- [44] O. Er-raji, L. Rustam, B. P. Kore, S. W. Glunz, P. S. C. Schulze, *ACS Appl. Energy Mater.* **2023**, *6*, 6183.